Polarization sensitive spectroscopy of charged quantum dots

E. Poem,* J. Shemesh, I. Marderfeld, D. Galushko, N. Akopian, and D. Gershoni
Department of Physics, The Technion-Israel Institute of Technology, Haifa 32000, Israel

B. D. Gerardot, A. Badolato, and P. M. Petroff
Materials Department, University of California Santa Barbara, Santa Barbara, California 93106, USA
(Received 25 May 2007; revised manuscript received 5 September 2007; published 4 December 2007)

We present an experimental and theoretical study of the polarized photoluminescence spectrum of single semiconductor quantum dots in various charge states. We compare our high resolution polarization sensitive spectral measurements with a many-carrier model which we developed for this purpose. The model considers both the isotropic and anisotropic exchange interactions between all participating electron-hole pairs. With this addition, we calculate both the energies and polarizations of all optical transitions between collective, quantum dot confined charge-carrier states. We succeed in identifying most of the measured spectral lines. In particular, the lines resulting from singly, doubly, and triply negatively charged excitons and biexcitons. We demonstrate that lines emanating from evenly charged states are linearly polarized. Their polarization direction does not necessarily coincide with the traditional crystallographic direction. It depends on the shells of the single carriers, which participate in the recombination process.

DOI: 10.1103/PhysRevB.76.235304 PACS number(s): 73.21.La, 78.67.Hc

I. INTRODUCTION

Quantum dots (QDs) are nanostructures which confine electrons and holes in all three dimensions. This confinement results in a discrete spectrum of single-carrier energy levels and spectrally sharp optical transitions between them. The photoluminescence (PL) spectrum of single self-assembled semiconductor QDs is usually composed of many discrete spectral lines. The variety of lines originates from optical transitions between various many-carrier configurations and different QD charge states.[1–5]

Several experimental techniques are used for identifying a given spectral line by associating it with a specific optical transition. These techniques include excitation intensity dependent PL spectroscopy, which distinguishes between single-exciton and multiexciton transitions,[6] and second order intensity cross-correlation measurements, which determines the temporal sequence by which the emission occurs in general,[6] and identifies radiative cascades in particular.[7,8] PL excitation[3,9] (PLE) as well as electro-PL[10] and magneto-PL[11,12] spectroscopies are used to further provide information regarding the QD's charge state during the optical transitions. Unfortunately, even when all of these methods are combined, occasionally, some lines still remain unidentified.[13]

Polarization sensitive PL and PLE spectroscopies have also been applied to aid in line identification. Most notably, the neutral exciton and neutral biexciton lines are split into two cross linearly polarized doublets,[14–16] while singly charged excitonic lines are unpolarized, and display large circular polarization memory[9,17,18] when excited quasiresonantly. In this work, we focus our studies on polarization sensitive PL spectroscopy of single semiconductor quantum dots. We carefully measure the polarization of the PL spectra under various excitation conditions. Our results are then compared with, and analyzed by, a theoretical many charge-carrier model. The method used for the calculation of the many-carrier states and optical transitions between them is the full-configuration-interaction method.[19] In particular, our model includes the electron-hole exchange interaction (EHEI).[11,20,21] We show that the model provides a very good understanding of the experimental measurements.

The paper is organized as follows: In Sec. II, we describe the sample and the experimental setup used for the polarization sensitive PL spectroscopy. In Sec. III, we describe the theoretical model, and in Sec. IV, we compare theoretical and experimental results. A short summary is given in Sec. V.

II. EXPERIMENTAL METHODS

A. Sample

The sample was grown by molecular beam epitaxy on a [001] oriented GaAs substrate. One layer of strain-induced InGaAs QDs was deposited in the center of a one wavelength GaAs spacer layer. The height and composition of the QDs were controlled by partially covering the InAs QDs by a 30 Å thick layer of GaAs and by subsequent 30 s growth interruption[22] to allow diffusion of In (Ga) atoms from (into) the strained islands. The growth resulted in $In_xGa_{1-x}As$ QDs whose exact shape, lateral size, composition, and strain profile are unknown.

The sample was not rotated during the growth of the strained layer, resulting in a variable density of QDs across the sample's surface.[6] The estimated density of QDs in the areas that were measured is 10^8 cm^{-2}.

The optical microcavity was formed by distributed Bragg reflecting (DBR) stacks of 25 and 11 periods of alternating AlAs and/or GaAs quarter wavelength layers below and above a GaAs spacer layer, respectively, giving a Q factor of ~500. The spacer layer was grown to a width close to the wavelength in matter of the light emitted from the QDs due to ground state electron-hole (e-h) pair recombinations (1λ cavity). The microcavity improves the efficiency of photon collection, but limits the energy in which photon collection is

possible. In particular, emission of photons with energies smaller than the microcavity mode energy is forbidden. Therefore, the density of QDs which emit efficiently is roughly 2 orders of magnitude lower than their actual density.[23] In order to electrically charge the QDs, a *p-i-n* junction was formed by *n* doping the substrate and the bottom DBR, and *p* doping the top DBR, while leaving the GaAs spacer intrinsic. An extra AlAs barrier was grown inside the GaAs spacer between the *p*-type region and the QDs. This barrier prolongs the hole's tunneling time into the QDs at forward bias and out of them at reverse bias, with respect to the tunneling time of the electron. This enables negative charging upon forward bias and positive charging upon reverse bias.

The top electrical contact of the sample was made of a semitransparent layer of indium-tin oxide in order to provide optical accessibility. The sample was not patterned or processed laterally to prevent obscuration of the QD emission and its polarization.

B. Optical characterization

For the optical measurements, we used a diffraction-limited low temperature confocal optical microscope.[2,24] The sample was mounted on a cold finger of a He-flow cryostat, maintaining a temperature of about ~20 K. A X60 *in situ* microscope objective was used in order to focus cw or pulsed laser light at normal incidence on the sample surface. The emitted light was collected by the same microscope objective. The objective was accurately manipulated in three directions using computer-controlled motors. The collected light was spatially filtered, dispersed by a 1 m monochromator, and detected by a nitrogen-cooled charge coupled device (CCD) array detector. The system provides diffraction-limited spatial resolution, both in the excitation and the detection channels, and spectral resolution of about 15 μeV per CCD camera pixel.

The polarization of the emitted light was analyzed by two computer-controlled liquid crystal variable retarders and a linear polarizer in front of the monochromator. The degree of polarization of the emitted light and its polarization state were deduced by six independent measurements of differently polarized spectra and calculation of the Stokes parameters.[25] Throughout this work, we use the symbol H (V) for linear light polarization along the $[1\bar{1}0]$ ([110]) crystallographic axis of the sample. These in-plane orientations are determined by cleaving. The symbol $D=\frac{1}{\sqrt{2}}(H+V)$ $[\bar{D}=\frac{1}{\sqrt{2}}(H-V)]$ is used for the 45° (−45°) diagonal polarization, while the symbol $R=\frac{1}{\sqrt{2}}(H+iV)$ $[L=\frac{1}{\sqrt{2}}(H-iV)]$ is used for the right (left) hand circular polarization.

A general state of polarization can be represented as a vector inside the Poincaré sphere. Figure 1 shows a vector in the Poincaré sphere and its relation to the shape and orientation of the polarization. In Fig. 2, we show the PL spectra from a single QD as a function of the voltage applied to the sample. The QD was excited by a cw 1.47 eV Ti:sapphire laser light. The current through the device as a function of the voltage is also shown. The specific structure of our sample is such that at forward biases (above ~7 V) the QDs

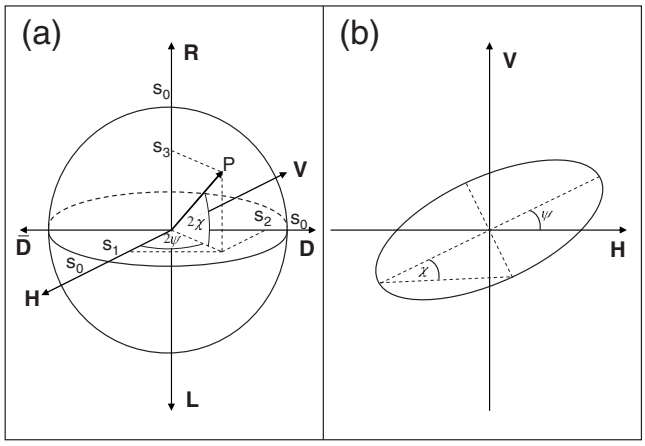

FIG. 1. (a) The polarization state represented as a vector **P** on the Poincaré sphere. (b) The same polarization state represented as the loci of points that the electric field of the light obtains, during one period, in a plane perpendicular to its propagation direction. $s_{0,\ldots,3}$ are the experimentally determined four Stokes coefficients (Ref. 25).

are negatively charged, as clearly evident by the abrupt step in the emission energy. This injection induced charging mechanism is similar to that reported earlier.[4,10] At large reverse biases, however, the QD is increasingly positively charged due to vast differences between the tunneling-out rates of electrons and holes.[9,26]

The spectral line identification in Fig. 2 is based on the order by which the lines appear and disappear as the voltage on the device increases. Information gained from excitation intensity dependence PL spectroscopy (not shown) and polarization sensitive spectroscopy (see below) is also used for this purpose.

In Fig. 3, we present the measured polarization sensitive spectra for the bias voltages indicated by horizontal lines in Fig. 2. We note here that the spectral shapes of the observed negatively charged lines and, in particular, the fine structure components of X^{-2}, XX^{-2}, and X^{-3} are similar to those observed also in previous works.[4,27]

In Fig. 3(a), the QD was, on average, neutral. The neutral as well as the singly negatively and singly positively charged exciton and biexciton spectral lines are observed. The corresponding polarization spectra projected on the linear H-V and on the linear D-$\bar{D}$ axes of the Poincaré sphere are shown in Fig. 3(b). The projections are calculated by subtracting the two cross-linearly polarized spectra divided by their sums. Division by zero is avoided by adding a constant equal to the standard deviation of the background noise to each spectrum. The projection on the R-L axis of the Poincaré sphere was zero to within our experimental uncertainty (not shown). From these two projections, the actual magnitude and direction of the linearly polarized lines can be straightforwardly determined. In Figs. 3(c) and 3(d), we present the PL spectrum and its linear polarization projections, respectively, for a bias voltage of 7.15 V at which the QD was, on average, negatively charged with two to three electrons.

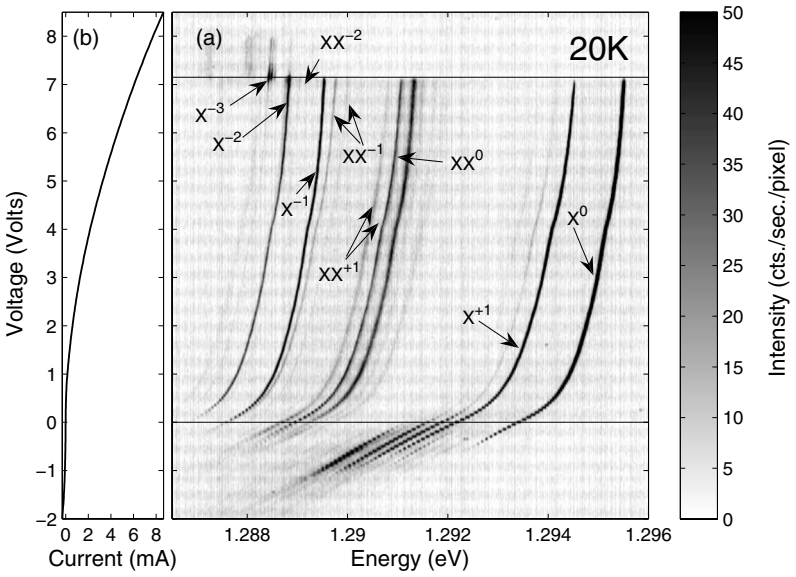

FIG. 2. (a) Measured PL spectra from a single SAQD as a function of the bias on the device. The QD was excited by 1.47 eV cw laser light. The various spectral lines are labeled by X (XX) for single (double) initial *e-h* pair occupation and a superscript which denotes the QD charge state during the recombination. The horizontal solid lines mark the voltages for which spectra are presented in Fig. 3. (b) The current through the device as a function of the bias voltage.

III. THEORETICAL MODEL

The model that we developed is a relatively simple many-carrier model which includes the electrostatic interactions between the QD confined charge carriers. Unlike previous, similar models[2,5,19] which neglected the EHEI, our model includes it. This interaction is indeed orders of magnitude smaller than the direct Columbic terms. Spectrally, it is only significant when the fine excitonic structure of the spectrum is considered. However, when the polarization spectrum is

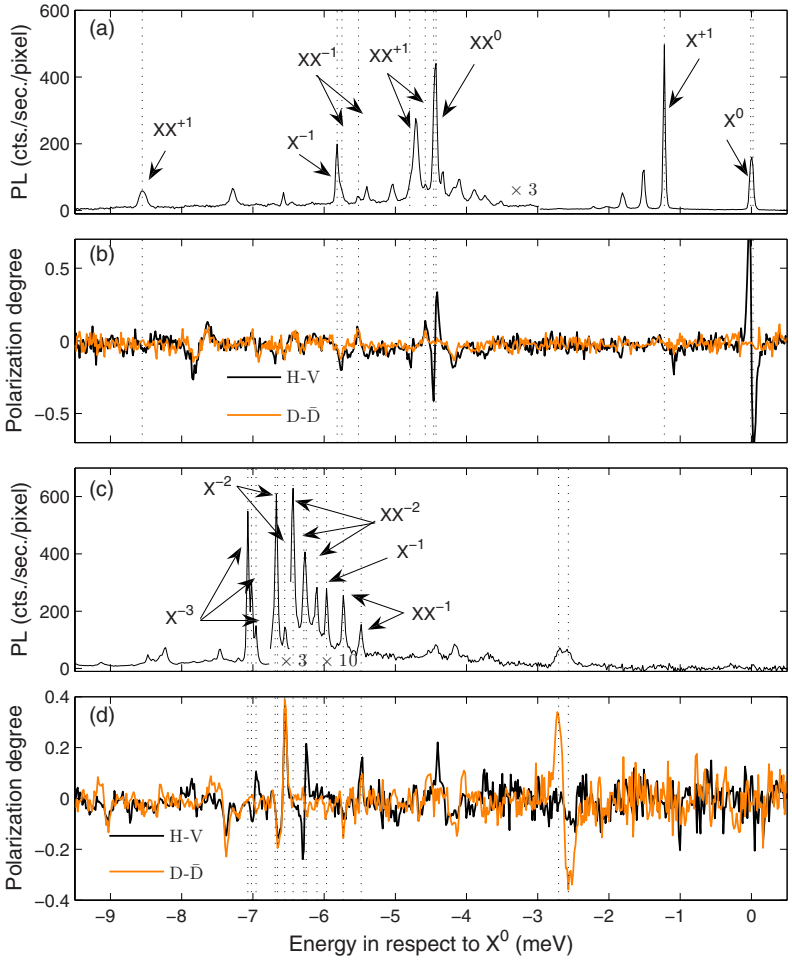

FIG. 3. (Color online) [(a) and (c)] Measured PL spectrum for bias voltages of 0 and 7.15 V, respectively. The energy is measured from the energy of the X^0 line. [(b) and (d)] PL polarization spectra for bias voltages of 0 and 7.15 V, respectively. The black (orange) lines present the polarization as projected on the H-V (D-D̄) axis of the Poincaré sphere. Vertical dash lines at various spectral lines are drawn to guide the eye.

TABLE I. The QD parameters used to calculate the single-carrier energies and envelope wave functions.

Parameter	Value	Units
QD shape	Rectangular slab	
QD size for the electron (Length × width × height)	244 × 232 × 34	Å
Hole/electron length ratio	0.72	
Electron effective mass	0.065[a]	m_0
Hole z-direction effective mass	0.34[a]	m_0
Hole in-plane effective mass	0.25	m_0
Electron potential offset	−324	meV
Hole potential offset	−108	meV
GaAs band gap	1.519[b]	eV
Band gap of QD material	1.087	eV
$In_{0.5}Ga_{0.5}As$ dielectric constant	13.8[b]	
E_p of $In_{0.5}Ga_{0.5}As$	25.5[a]	eV

[a]Reference 31.
[b]Reference 32.

considered, this anisotropic interaction[20,28,29] is by far the leading term.

Our model is constructed as follows: We first solve a single-carrier problem for the electron and for the hole in the QD. In this manner, we obtain a consistent set of single charge-carrier energies and associated wave functions. We then use this set of energies and wave functions in order to construct a many-carrier second quantization Hamiltonian, which includes the electrostatic interaction between the confined carriers. In particular, we consider the EHEI which is introduced into our model using a semiphenomenological approach. The many-body Hamiltonian is then diagonalized, thus obtaining the collective many-carrier energies and wave functions. We then use the dipole approximation to calculate the optical transitions between the many-carrier states for a given light polarization. From these calculations, we finally construct the polarization sensitive emission spectrum, which is used for comparison with the experimental measurements.

A. Single-carrier problem

The single-carrier energies and wave functions are calculated using the slowly varying envelope-function approximation (SVEFA).[30] We use one (doubly Kramers degenerate) band for the electron and one band for the hole without band mixing ("one-band SVEFA"). This approximation results in two independent Schrödinger equations for the envelope functions of the electron and that of the hole. The potential of the QD is approximated by a finite three-dimensional potential well in the form of a rectangular slab, with the long (short) side oriented along the H (V) direction, and with different dimensions and offsets for the two types of carriers. The parameters that we used are listed in Table I. We solved the differential equations numerically, using the finite differences method, thus obtaining the single particle eigenenergies and envelope wave functions.

B. Many-carrier Hamiltonian

The second quantization many-carrier Hamiltonian for the QD containing both electrons and holes is given by[2,19]

$$\hat{H} = \hat{H}_0 + \hat{H}_{ee} + \hat{H}_{hh} + \hat{H}_{eh}, \tag{1}$$

where $\hat{H}_0$ is the single-carrier Hamiltonian, $\hat{H}_{ee}$ ($\hat{H}_{hh}$) is the electron-electron (hole-hole) interaction Hamiltonian, and

$$\hat{H}_{eh} = \sum_{i_1,i_4,j_2,j_3} (-C^{ehhe}_{i_1,j_2,j_3,i_4} + C^{hehe}_{j_2,i_1,j_3,i_4}) \hat{a}^\dagger_{i_1} \hat{b}^\dagger_{j_2} \hat{b}_{j_3} \hat{a}_{i_4} \tag{2}$$

is the electron-hole interaction Hamiltonian. The electron creation operator $\hat{a}^\dagger_i$ and the hole creation operator $\hat{b}^\dagger_j$ separately satisfy the regular fermionic anticommutation relations. The quantities of the form $C^{p_1p_2p_3p_4}_{n_1,n_2,n_3,n_4}$, where $p_{1,\ldots,4}$ can be either e (for electron) or h (for hole), and the indices $n_{1,\ldots,4}$ run over the appropriate states, are the Coulomb interaction integrals.

Computation is only feasible with a limited number of single-carrier states. Therefore, only the first 12 lowest energy electron and hole states are usually considered in our calculations.

For the single-carrier wave functions which are calculated using the SVEFA, the Coulomb integrals can be separated into long-range (inter-unit-cell) and short-range (intra-unit-cell) integrals. The long-range integral can be expanded into a Taylor series in $\vec{r}_1 - \vec{r}_2 - (\vec{R}_1 - \vec{R}_2)$, where $\vec{R}_{1(2)}$ is the lattice vector nearest to the position vector $\vec{r}_{1(2)}$. In most cases, the zeroth order of that series is much larger than the other orders, and also larger than the short-range integral.[30] For the one-band SVEFA, the zeroth order of the long-range interaction is given by[30]

$$C^{p_1p_2p_3p_4}_{n_1,n_2,n_3,n_4} = \delta_{p_1,p_4}\delta_{p_2,p_3}\delta_{S_{n_1},S_{n_4}}\delta_{S_{n_2},S_{n_3}} \int\int d^3r_1 d^3r_2 \times \phi^{p_1}_{n_1}{}^*(\vec{r}_1)\phi^{p_2}_{n_2}{}^*(\vec{r}_2)\frac{e^2}{\epsilon|\vec{r}_1 - \vec{r}_2|}\phi^{p_2}_{n_3}(\vec{r}_2)\phi^{p_1}_{n_4}(\vec{r}_1), \tag{3}$$

where $\phi^p_n(\vec{r})$ is the envelope function of the nth state of a single carrier of type p, e is the electron charge, ϵ is the dielectric constant of the QD material, and S_n is the (pseudo) spin of state n.

The rectangular slab shape of our model QD is symmetric under reflections about planes perpendicular to its main symmetry axes. Therefore, single-carrier envelope functions are either odd or even under these reflections. The term $\frac{1}{|\vec{r}_1 - \vec{r}_2|}$ is even under the application of the same reflection for both $\vec{r}_1$ and $\vec{r}_2$. Therefore, the parity of the integrand in Eq. (3) under such a "double reflection" is determined by the parities of the envelope functions only. Whenever the integrand is odd under a double reflection, the integral vanishes. We use these symmetry considerations in order to reduce the required computation resources.

C. Electron-hole exchange interaction

The zeroth order term in the long-range EHEI, $C^{hehe}_{j_2,i_1,j_3,i_4}$ [Eq. (3)], equals zero. Therefore, higher order terms in the long-range as well as the short-range exchange integral must be considered.[29,33]

The pseudospin structure of the EHEI for the lowest energy envelope functions is deduced from symmetry considerations (the method of invariants).[11,20] The SVEFA requires that the same considerations hold also for any other combination of envelope functions.[29] Thus, we express the electron-hole-exchange terms $C^{hehe}_{j_2,i_1,j_3,i_4}$ as follows:

$$C^{hehe}_{j_2,i_1,j_3,i_4} = \frac{1}{2}\begin{pmatrix} \Delta_0^{nj_2,ni_1,nj_3,ni_4} & \Delta_1^{nj_2,ni_1,nj_3,ni_4} & 0 & 0 \\ \Delta_1^{nj_2,ni_1,nj_3,ni_4*} & \Delta_0^{nj_2,ni_1,nj_3,ni_4} & 0 & 0 \\ 0 & 0 & -\Delta_0^{nj_2,ni_1,nj_3,ni_4} & \Delta_2^{nj_2,ni_1,nj_3,ni_4} \\ 0 & 0 & \Delta_2^{nj_2,ni_1,nj_3,ni_4*} & -\Delta_0^{nj_2,ni_1,nj_3,ni_4} \end{pmatrix}, \tag{4}$$

where ni_k represents the index of the envelope function belonging to state number i_k. The e-h pseudospin base for the matrix are the functions $\{|\downarrow\Uparrow\rangle, |\uparrow\Downarrow\rangle, |\uparrow\Uparrow\rangle, |\downarrow\Downarrow\rangle\}$.

The terms Δ_0 and Δ_2 are mainly affected by the short-range interaction.[20,29] This intra-unit-cell interaction is not sensitive to the details of the slowly varying envelope wave functions.[29] Therefore, we assume that all the nonvanishing $\Delta_0^{n_2,n_1,n_3,n_4}$ and $\Delta_2^{n_2,n_1,n_3,n_4}$ terms have the same values, Δ_0 and Δ_2, respectively. The values that we used were chosen such that the calculated X^0 spectrum would fit the magneto-PL measured X^0 spectrum.[12] Since the short-range interaction is even under double reflections,[29] the symmetry considerations which aid in identifying the vanishing Coulomb integrals apply also in identifying the vanishing EHEI terms Δ_0 and Δ_2.

The $\Delta_1^{n_2,n_1,n_3,n_4}$ integrals are mainly affected by the second order terms in the expansion of the long-range interaction, which are given by[20,29]

$$\frac{1}{2}\Delta_1^{n_2,n_1,n_3,n_4} = \int\int \phi_h^{n_2*}(\vec{r}_1)\phi_e^{n_1*}(\vec{r}_2)\frac{e^2\vec{\mu}^\dagger_{\downarrow,\Uparrow}(\mathbb{1}-3\hat{n}\hat{n}^\dagger)\vec{\mu}_{\uparrow,\Downarrow}}{\varepsilon|\vec{r}_1-\vec{r}_2|^3} \times \phi_h^{n_3}(\vec{r}_2)\phi_e^{n_4}(\vec{r}_1)d^3r_1d^3r_2, \tag{5}$$

where $\hat{n}$ is a unit vector in the direction of $\vec{r}_1-\vec{r}_2$, $\mathbb{1}$ is the 3×3 unit matrix, and $\vec{\mu}_{\uparrow,\Downarrow}$ is the valence-conduction band dipole matrix element. The dipole matrix element $(\vec{\mu})$ is related to the momentum matrix element $(\vec{M})$ through the particle's mass and the energy difference between the dipole states[34] (the band gap energy E_g),

$$\vec{\mu}_{\uparrow,\Downarrow(\downarrow,\Uparrow)} = \frac{-i\hbar}{m_0E_g}\vec{M}_{\uparrow,\Downarrow(\downarrow,\Uparrow)}, \tag{6}$$

where the conduction-valence band momentum matrix elements are given by[28,31]

$$\vec{M}_{\uparrow,\Uparrow} = \vec{M}_{\Downarrow,\downarrow} = \vec{0}, \tag{7}$$

$$\vec{M}_{\uparrow,\Downarrow(\downarrow,\Uparrow)} = \frac{i}{2}\sqrt{m_0E_p}(1,(-)i,0), \tag{8}$$

where E_p is the bulk material conduction-valence band interaction energy,[31,35] and the spin quantization axis is chosen along the [001] (or z) direction. For compatibility with the experimentally defined axes, we choose the major axis of the QD, believed to be along the $[1\bar{1}0]$ crystallographic axis,[14] as the x (or H) direction.

Substituting Eqs. (6)–(8) into Eq. (5) yields

$$\Delta_1^{n_2,n_1,n_3,n_4} = \frac{3e^2\hbar^2E_p}{2\epsilon m_0E_g^2}\int\int \phi_h^{n_2*}(\vec{r}_1)\phi_e^{n_1*}(\vec{r}_2) \times \frac{(y_1-y_2)^2-(x_1-x_2)^2+2i(x_1-x_2)(y_1-y_2)}{[(x_1-x_2)^2+(y_1-y_2)^2+(z_1-z_2)^2]^{5/2}} \times \phi_h^{n_3}(\vec{r}_2)\phi_e^{n_4}(\vec{r}_1)d^3r_1d^3r_2. \tag{9}$$

One can now, in principle, compute these integrals using the single-carrier envelope wave functions that were numerically obtained earlier. This approach demands a lot of computation resources in order to obtain reliable accuracy. Therefore, we choose to approximate the wave functions analytically by using in-plane harmonic oscillator functions[36] instead of the numerical ones (see Appendix A). With these approximations, the six dimensional integrals are reduced into five analytical ones.[37] The nonanalytical integral can be easily calculated numerically. Alternatively, for a nearly round QD, this integral can be expanded into a power series in the aspect ratio of the model QD, from which only terms up to the linear order can be kept. This approach provides also important insight. The result of this derivation for $\Delta_1^{1,1,1,1}$ is

$$\Delta_1^{1,1,1,1} = \frac{3\sqrt{\pi}e^2\hbar^2E_p(\xi-1)}{8\epsilon m_0E_g^2(l_x^e)^3\xi^2\beta\sqrt{1+\beta^2}}, \tag{10}$$

where l_x^e is the characteristic length of the electron (Gaussian) wave function in the x direction (see Appendix A), $\beta=0.72$ is the ratio between the characteristic length of the hole wave function to that of the electron, and $\xi=0.96$ is the

TABLE II. Calculated, measured, and estimated electron-hole exchange interaction terms (in μeV). The measured and estimated terms were used for calculating the PL spectra. The calculated ratios are given in terms of the hole/electron length ratio β and the aspect ratio ξ, for $|1-\xi| \ll 1$.

Parameter	Used in fit	Calculated	Ratio to $\Delta_1^{1,1,1,1}$
Δ_0	207		
Δ_2	21		
$\Delta_1^{1,1,1,1}$	−25	−15	
$\Delta_1^{1,2,1,2}$	196	118	$\frac{\beta^2}{1+\beta^2}\frac{2\xi-1}{\xi-1}$
$\Delta_1^{1,3,1,3}$	−222	−133	$\frac{\beta^2}{1+\beta^2}\frac{\xi-2}{\xi-1}$
$\Delta_1^{1,4,1,4}$	−6.4	−3.8	$\frac{\beta^4}{(1+\beta^2)^2}\frac{41-6\xi}{16}$
$\Delta_1^{1,5,1,5}$	232	139	$\frac{1}{2}+\frac{\beta^2}{1+\beta^2}\frac{1}{\xi-1}+\frac{\beta^4}{(1+\beta^2)^2}\frac{61\xi-45}{32(\xi-1)}$
$\Delta_1^{2,1,2,1}$	379	227	$\frac{1}{1+\beta^2}\frac{2\xi-1}{\xi-1}$
$\Delta_1^{2,2,2,2}$	119	71	$\frac{\beta^2}{(1+\beta^2)^2}\frac{61\xi-45}{16(\xi-1)}$
$\Delta_1^{2,3,2,3}$	−12	−7.4	$\frac{\beta^2}{(1+\beta^2)^2}\frac{41-6\xi}{16}$
$\Delta_1^{2,2,2,3}$	$71i$	$42i$	$i\frac{\beta^2}{(1+\beta^2)^2}\frac{9-\xi}{16(\xi-1)}$
$\Delta_1^{1,2,1,3}$	$209i$	$125i$	$i\frac{\beta^2}{1+\beta^2}\frac{\xi+1}{2(\xi-1)}$

length ratio between the short and long sides of the rectangle (the aspect ratio).

For l_x^e=72 Å, which gives the same s-p_x energy separation for the electrons as the numerical wave functions, we calculated the Δ_1 terms, which we list in Table II. In the table, we also list the values that we could directly deduce from the measured fine structure splitting of the X^0 and X^{-2} lines ($\Delta_1^{1,1,1,1}$ and $\Delta_1^{1,2,1,2}$, respectively). The agreement, as can be seen in the table, is remarkable.

We note that the ratios $\Delta_1^{n_2,n_1,n_3,n_4}$ to $\Delta_1^{1,1,1,1}$ can be quite large for small deviations from the symmetrical case. In particular, there are significant sign variations between the various terms. The expressions for these ratios as functions of β and ξ (for $|1-\xi| \ll 1$) are also given in Table II.

D. Optical transitions: Polarization selection rules

The optical transition operator in the dipole approximation is expressed as[19]

$$\hat{\vec{P}} = \sum_{i,j} \vec{p}_{ij} \hat{a}_i \hat{b}_j. \tag{11}$$

Under the one-band SVEFA, the transition momentum vector $\vec{p}_{ij}$ is given by

$$\vec{p}_{ij} = \vec{M}_{S_j,S_i} \int \phi_i^{e*}(\vec{r}) \phi_j^h(\vec{r}) d^3r. \tag{12}$$

The momentum matrix elements $\vec{M}_{S_j,S_i}$ are given explicitly by Eqs. (7) and (8).

The rate of an optical transition[38] centered at an energy ε, for a certain polarization $\vec{e}$, is given by

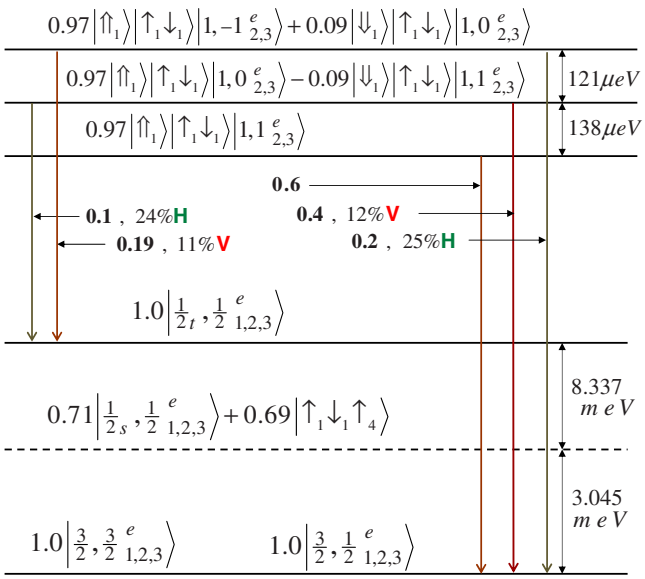

FIG. 4. (Color online) Schematic description of the calculated many-carrier energy levels, and their spin wave functions, in which an optical transition between them results in the X^{-3} spectral lines. Each transition rate (in units of the total X^0 rate) and its degree of polarization are indicated (if absent, the transition is unpolarized). Only one of the two Kramers states is shown for each level (for notation, see Appendix B). The number before each component indicates its amplitude. Components which are irrelevant to the polarization degree and have amplitudes below 0.1 are not included.

$$\Gamma_{\vec{e}}(\varepsilon) = \frac{4\alpha n \varepsilon}{3\hbar m_0^2 c^2} \sum_{i,f} |\langle f|\vec{e}\cdot\hat{\vec{P}}|i\rangle|^2 \delta_{\varepsilon,\varepsilon_i-\varepsilon_f} F_i, \tag{13}$$

where $\alpha = \frac{e^2}{\hbar c} \approx \frac{1}{137}$ is the fine structure constant, and n is the refraction index of the QD material. The indices i and f run over all initial states $|i\rangle$ and final states $|f\rangle$. ε_i (ε_f) is the energy of the initial state $|i\rangle$ (final state $|f\rangle$). F_i is the population probability of the initial state $|i\rangle$. For the bright neutral exciton transitions, we calculate

$$|\langle 0|\hat{x}\cdot\hat{\vec{P}}|X_H^0\rangle|^2 = |\langle 0|\hat{y}\cdot\hat{\vec{P}}|X_V^0\rangle|^2 = \frac{m_0 E_p}{2}(1.44). \tag{14}$$

The other two transitions from the bright states and the transitions from the "dark" excitonic states vanish. Assuming equal population probabilities for the bright and dark X^0 states, we get a total X^0 rate of $(0.78\ \text{ns})^{-1}$, in agreement with the measured lifetime.[7] The calculated rates of all other optical transitions are given in units of this total X^0 rate.

For example, in Fig. 4 we present a diagram of the calculated many-carrier energy levels and the optical transitions between them, which lead to the spectrum resulted from excitonic transitions in a triply negatively charged QD (X^{-3}). As can be deduced from Fig. 4, the X^{-3} line results from three initial levels (each doubly Kramers degenerate). These levels contain mainly the following single-carrier states: one s-shell hole, two s-shell electrons, and one p_x and one p_y electron, where the p-shell electrons are in their triplet configurations. These open shell configurations are the lowest in

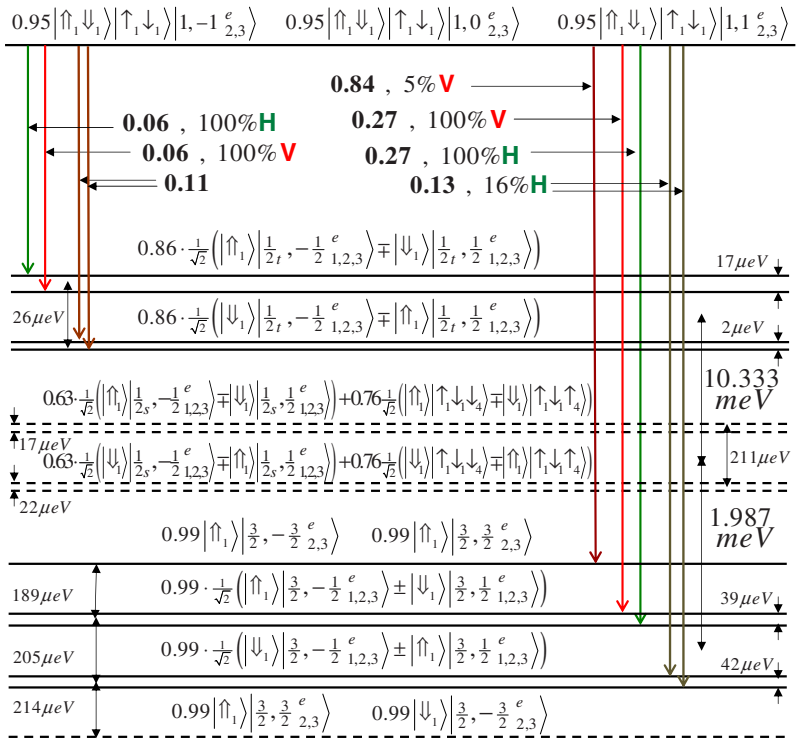

FIG. 5. (Color online) Schematic description of the calculated many-carrier energy levels, and their spin wave functions, in which an optical transition between them results in the XX^{-2} spectral lines. Each transition rate (in units of the total X^0 rate) and its degree of polarization are indicated (if absent, the transition is unpolarized). All states are shown (for notation, see Appendix B). The number before each component indicates its amplitude. Components which have amplitudes below 0.1 are not included.

energy, since the energy difference between the p_x and p_y single electron states is smaller than their exchange interaction. The degeneracy between the triplet configurations is removed by the EHEI with the hole. Our experimental data can only be explained with these open p-shell occupation in mind (see below).

The final states are mainly composed of three single electron states: one in the s shell, one in the p_x shell, and one in the p_y shell. The expected eightfold degeneracy is partially removed by the electron-electron exchange interaction, which leaves a fourfold degenerate ground state (we found no experimental evidence for an anisotropic e-e exchange interaction[9] which would have further reduced this degeneracy). The calculated optically allowed transitions between the initial and final states and their polarization selection rules are given in Fig. 4. The highest energy transition is finely structured from three lines with intensity ratios of approximately 3:2:1. These intensities were previously deduced using a simple model by Urbaszek *et al.*[4]

If the ground p shell was occupied by two electrons, the X^{-3} transitions would have generated a single almost unpolarized spectral line, very similar to that due to the X^{-1} transitions. This is in clear contradiction with the measurements presented in Fig. 3, Fig. 8, and previous measurements on similar QDs.[4,27]

Another example is provided in Fig. 5, where we show the levels' diagram and optical transitions, which result in the biexciton recombination in a doubly negatively charged QD (XX^{-2}).

Here, the initial states are mainly composed of the same single-carrier states as the initial states of the X^{-3}, except for the addition of one more s-shell hole. Unlike the X^{-3}, the paired s-shell holes do not remove the degeneracy of the triplet configuration of the p-shell electrons. Similarly, the final states are mainly composed of the same single electron states as the final states of the X^{-3}, except for an additional one s-shell hole. The EHEI between the unpaired hole and the electrons completely removes the degeneracy between the electron states. As a result, there are eight low energy states (the energy differences between the lowest and between the highest pairs of states are too small to be noted) to six of which optical transitions are allowed. Similar to the case of the X^{-3}, the optical spectrum is finely structured from three pairs of lines with total intensity ratios of approximately 3:2:1 as previously deduced by the simple considerations of Urbaszek *et al.*[4] A major difference between the two examples is in their polarization selection rules. In the first case (X^{-3}), the total spin is half-integer and Kramers degeneracy prevails. Therefore, only partial linear polarization is expected. In the second case (XX^{-2}), the total spin is an integer. In this case, full linear polarization is expected, just like in the case of the neutral single exciton. Indeed, the intermediate pair of spectral lines is fully polarized along the QD's primary axes.

Similar diagrams for less complicated transitions were discussed in previous works.[11,21,39] In these works, simpler models were used. These models are sufficient only when the EHEIs are much smaller than any other interaction. In Figs. 6(a) and 6(c), we show the calculated spectrum for various charge states. The corresponding H-V polarization projections are shown in Figs. 6(b) and 6(d), respectively.

Within our simple, one-band model, the calculated D-$\bar{\text{D}}$ (and, of course, the R-L) projections vanish, and therefore, they are not shown. For the calculations, equal probabilities for excitons and biexcitons in all charge states were assumed.[40] In the calculations, only initial configurations within 1 meV (compatible with the experiments' temperature) above the ground state were considered.

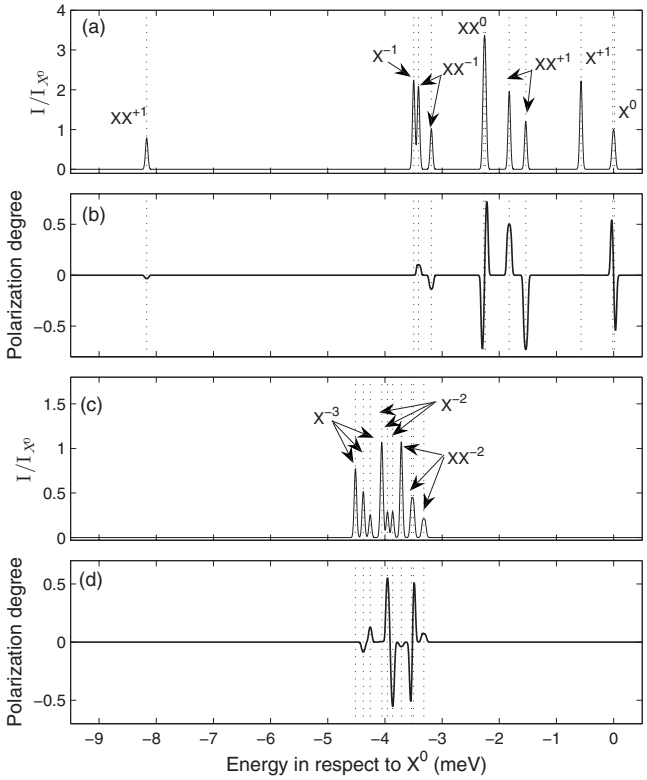

FIG. 6. [(a) and (c)] Calculated PL spectra and [(b) and (d)] their polarization projections on the H-V axis for various single QD excitonic transitions. Vertical dash lines at various spectral lines are drawn to guide the eye.

The calculated lines are convoluted with 50 μeV broad Gaussians to account for the spectral diffusion.[7] In the calculation of the polarization projections, a constant background of 3.5% of the maximal intensity is added to both cross-linearly polarized spectra. This is done in order to mimic the effect of background noise on the measured spectra (see Sec. II).

IV. COMPARISON BETWEEN EXPERIMENTAL MEASUREMENTS AND MODEL CALCULATIONS

In Fig. 7, we compare between the measured and calculated spectral positions of various lines. We note that the spectrum produced by our simple model correlates with the experimentally measured one in the energy order of the various spectral lines. The calculated energy differences between the various lines, however, are in most cases smaller than those measured. Specifically, the calculated energy differences between the exciton and biexciton and between the positive and negative trions (X^{+1} and X^{-1}, respectively) are smaller than the measured ones. This is probably a consequence of the relative simplicity of our single band model[41] and the lack of information about the exact shape, strain, and composition of the QDs. With our model's limitations, we found it hard to simultaneously fit the biexciton binding energy and the difference between the positive and negative trion transitions.

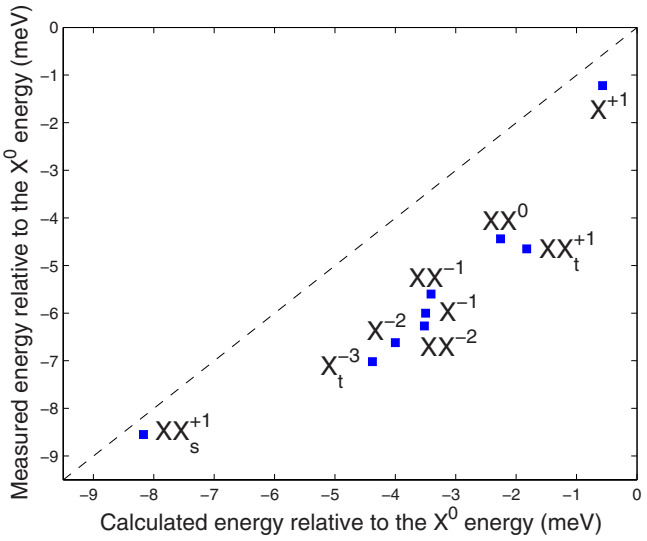

FIG. 7. (Color online) A comparison between measured and calculated spectral positions of a few lines. The dashed line is the equality line. The size of the markers represents the experimental error.

In Fig. 8, we compare the measured and calculated polarized fine structure of various spectral lines, while in Fig. 9, we compare the measured and calculated linear polarization spectra for these spectral lines. We note in Figs. 8 and 9 that the measured fine structures are reproduced quite nicely by our model calculations. In particular, the calculated number of fine structure components, their relative intensities, and their polarizations correlate with the measured values.

On the other hand, while the calculated polarization spectra are always polarized along the H-V axis of the Poincaré sphere, the measured ones are sometimes rotated. Few specific lines (see below) are polarized along the $(V+\bar{D})$-(H +D) axis.

The calculated energy differences between the fine structure components of a given spectral line are sometimes larger than the measured values. Particularly, the calculated fine structure splittings between the components of the X^{-3} line and the calculated splitting between the unpolarized and polarized doublets of the X^{-2} line are larger than the measured ones. We believe that this may be a consequence of the Δ_0 dependencies on the envelope wave functions, which are neglected in our model.

In the absence of polarization memory (which requires quasiresonant polarized excitation[9]), and in the absence of magnetic field, the theory predicts that the spectral lines can only present linear polarizations. This is what we observed experimentally as well. In the theoretical model, the linear polarization can only be oriented along the main axes of the QD, which are usually along the crystalline directions $[1\bar{1}0]$ and [110],[14] which we denote by H and V, respectively. In the experiment, however, we found that some spectral lines are polarized along other directions. The polarization appears in *three* sets of orthogonal axes: The measured polarization of the neutral exciton line is indeed along the H-V axis of the Poincaré sphere. A few other lines, notably the neutral biex-

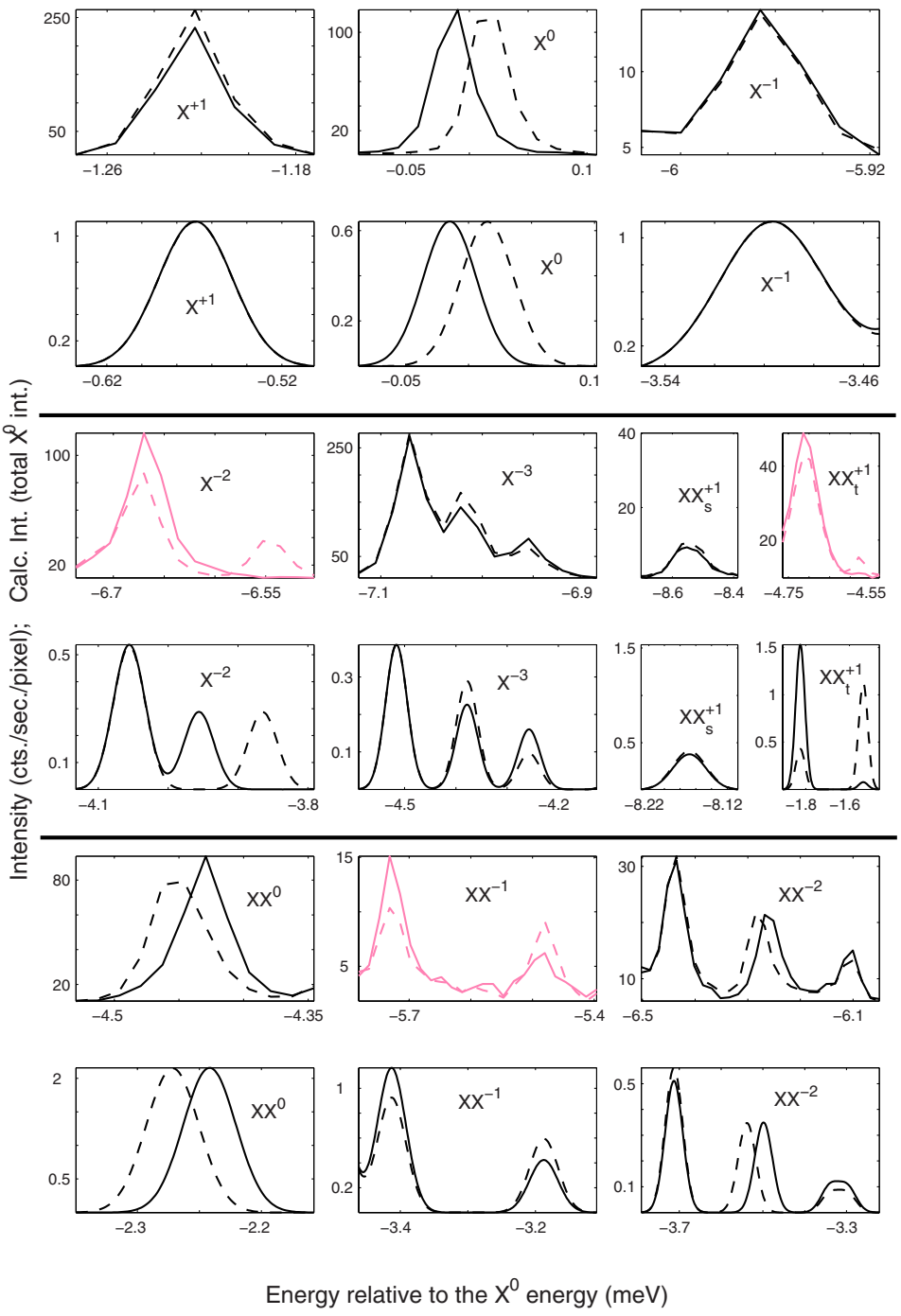

FIG. 8. (Color online) Measured (top panel in each pair) and calculated (bottom panels) high resolution polarization sensitive PL spectra of various spectral lines. The solid (dashed) black line represents H (V) polarized spectrum, while the solid (dashed) pink line represents the V+$\bar{\text{D}}$ (H+D) polarized spectrum.

citon, the doubly charged biexciton, and the triply charged exciton, are also polarized along this axis. Their degree of polarization is somewhat smaller than that of the X^0 lines due to the unpolarized spectral background that they ride on. Few other spectral lines are polarized along an axis which is rotated clockwise by 135° relative to the H-V axis of the Poincaré sphere.

This polarization axis, which roughly coincides with the $\frac{1}{\sqrt{2}}(\text{V}+\bar{\text{D}})$ ([120]) and the $\frac{1}{\sqrt{2}}(\text{H}+\text{D})$ ([$2\bar{1}0$]) crystalline directions, appears only in lines associated with configurations which contain one unpaired p_x carrier (either electron or hole): X^{-2}, XX^{-1}, and XX^{+1}. Careful inspection of the unevenly polarized spectra of the X^{-2} line presented by Ediger *et al.*[27] leads to the same conclusion. Unfortunately, they did not fully measured the polarization state of the line.

For other configurations, which contain only s carriers or either closed shells or two unpaired p carriers (p_x and p_y), the polarization is along the H-V axis. In addition, we sometimes observe lines which are polarized along the D-$\bar{\text{D}}$ axis as well. Such a spectral line is seen in Fig. 3(d), at energy of −2.6 meV relative to the X^0 line. This relatively weak doublet may result from pair recombination in doubly negatively charged QD as deduced from its voltage dependence.

These observations are not reproduced by the simple model that we present, probably since the model, ignores the underlying crystal. For example, in the single band model,

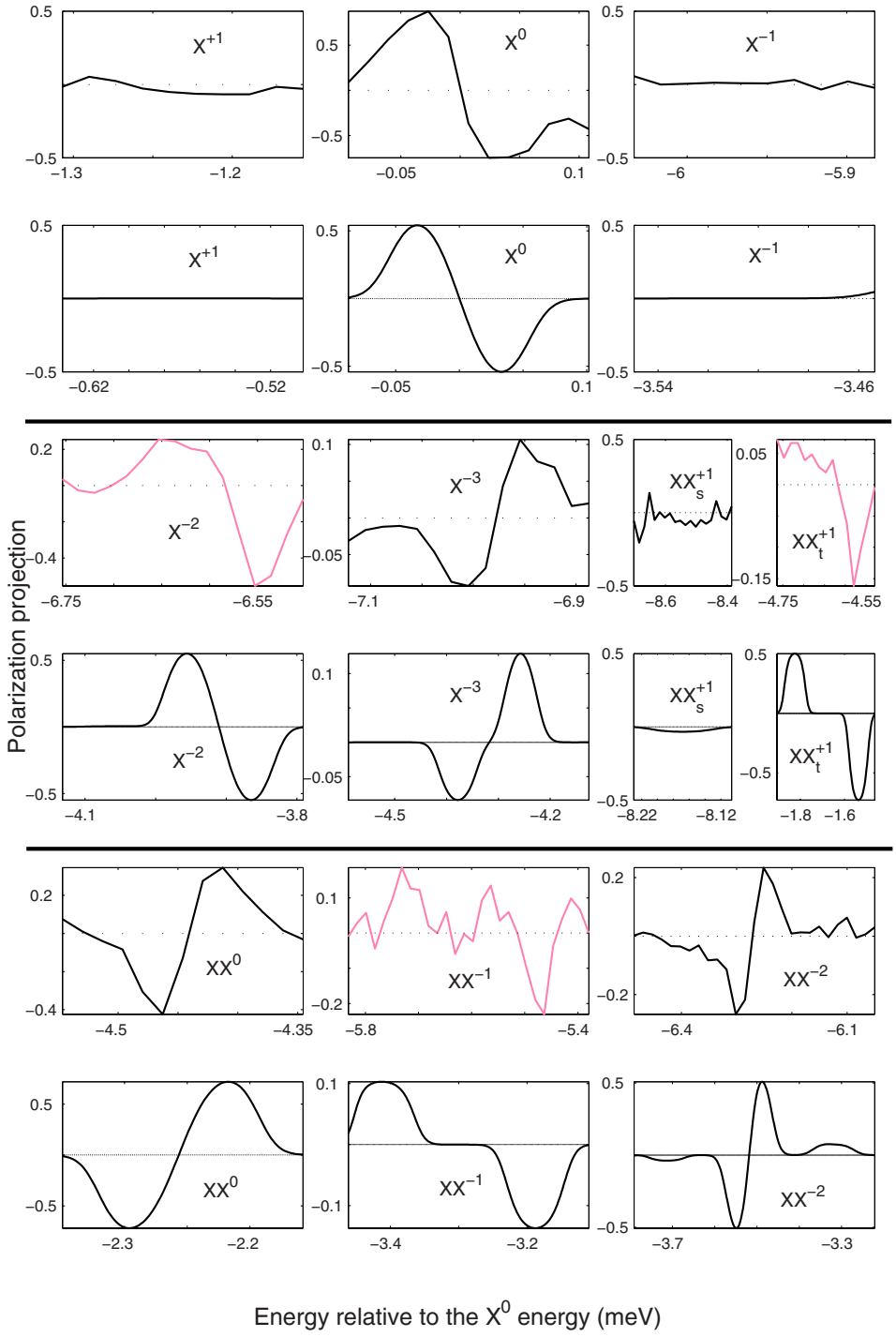

FIG. 9. (Color online) Measured (top panels) and calculated (bottom panels) linear polarization spectra of various spectral lines. Black (pink) solid lines represent projections along the H-V [(V+D)-(H+D)] axis of the Poincaré sphere.

the polarization due to recombination of a p_x shell e-h pair is the same as that of a p_y pair, which is clearly not the case.

We rule out another possible explanation[42] expected in a nearly p-shell degenerated QD. In such a QD, where the p_x-p_y splitting is comparable to or smaller than the EHEI, configurations containing an unpaired p_x carrier and those containing an unpaired p_y carrier are mixed.[42] This mixing can indeed lead to recombination in linear polarizations along axes different from the primary axes of the QD. This is not the case here, since for nearly degenerate QDs, the fine structures of the X^{-2}, XX^{-1}, and XX^{+1} transitions should contain twice the number of fine structure components than that actually observed.

One straightforward way to include the lattice will be to solve the single electron problem using a multiband approach.[31,43] Such a model is absolutely necessary for calculating the polarization selection rules in highly positively charged QDs. There, the complicated nature of the p-shell holes is not likely to be captured by a one-band model. The polarization degree of the highly positively charged QD emission lines (identified by their voltage dependence) that we measured was marginal, while our single band model

yields polarizations similar to those of the negatively charged QD lines. We believe that this discrepancy results from the inadequacy of the single band model. In addition, we note that the highly positively charged QD lines were all measured under large electrostatic fields, which, for now, were not considered in our model.

V. SUMMARY

We presented detailed polarization sensitive spectroscopy of single QDs in various charge states. We developed a many-carrier model based on single band, envelope-function approximation, which includes the isotropic and anisotropic electron-hole exchange interactions for the analysis of the measured data. We calculated the PL spectrum with its fine structure and polarizations for the exciton and biexciton optical transitions in neutral, singly positively, and singly, doubly, and triply negatively charged QDs. The calculations are favorably compared with the measured polarization sensitive PL spectra.

However, while our model can only reproduce polarizations along the main axes of the QD, the experimental data display polarizations oriented along other directions as well. This indicates, probably, that the one-band-based model is too simple to describe this observation.

ACKNOWLEDGMENTS

The research was supported by the US-Israel Binational Science Foundation (BSF), the Israeli Science Foundation (ISF), and the Russell Berrie Nanotechnology Institute (RBNI) at the Technion. We acknowledge fruitful correspondence with E. L. Ivchenko.

APPENDIX A: ANALYTICAL WAVE FUNCTIONS USED IN THE CALCULATION OF THE Δ_1 INTEGRALS

As model functions we used the following functions:

$$\phi_1^p = |0,0\rangle_p, \quad \phi_2^p = |1,0\rangle_p, \quad \phi_3^p = |0,1\rangle_p,$$

$$\phi_4^p = |1,1\rangle_p, \quad \phi_5^p = |2,0\rangle_p, \quad \phi_6^p = |0,2\rangle_p.$$

The kets of the form $|n_x,n_y\rangle_p$ stand for the two-dimensional elliptic harmonic oscillator functions:

$$\langle x,y|n_x,n_y\rangle_p = \frac{H_{n_x}\left(\frac{x}{l_p^x}\right)H_{n_y}\left(\frac{y}{l_p^y}\right)}{\sqrt{2^{(n_x+n_y)}n_x!n_y!\pi l_p^x l_p^y}} e^{-(1/2)[(x/l_p^x)^2+(y/l_p^y)^2]},$$

where p is the charge-carrier index (either e or h), $l_p^{x(y)}$ is a characteristic length along the x (y) direction, $n_{x(y)}$ is the quantum number associated with the x (y) direction, and $H_{n_{x(y)}}$ is the Hermite polynomial of order $n_{x(y)}$. The aspect ratio ξ and the hole/electron length ratio β are defined as $\xi = \frac{l_e^y}{l_e^x} = \frac{l_h^y}{l_h^x}$ and $\beta = \frac{l_h^x}{l_e^x} = \frac{l_h^y}{l_e^y}$.

TABLE III. The abbreviations used to write the state vectors. $\uparrow_j$ ($\Downarrow_j$) stands for an electron (hole) with envelope-function number j and pseudo-spin-up (down). $j=1$ is the s state, $j=2$ is the p_x state, $j=3$ is the p_y state, $j=4$ is the d_{xy} state, $j=5$ is the d_{xx} state, and $j=6$ is the d_{yy} state. Where two or more of i, j, and k appear together, it is assumed that $i \neq j \neq k$.

Abbreviation	Full form
$\|0,0\,{}^e_{ij}\rangle$	$\frac{1}{\sqrt{2}}(\|\uparrow_i\downarrow_j\rangle - \|\downarrow_i\uparrow_j\rangle)$
$\|1,0\,{}^e_{ij}\rangle$	$\frac{1}{\sqrt{2}}(\|\uparrow_i\downarrow_j\rangle + \|\downarrow_i\uparrow_j\rangle)$
$\|1,1\,{}^e_{ij}\rangle$	$\|\uparrow_i\uparrow_j\rangle$
$\|1,-1\,{}^e_{ij}\rangle$	$\|\downarrow_i\downarrow_j\rangle$
$\|\frac{3}{2},\frac{1}{2}\,{}^e_{ijk}\rangle$	$\frac{1}{\sqrt{3}}(\|\uparrow_i\uparrow_j\downarrow_k\rangle + \|\uparrow_i\downarrow_j\uparrow_k\rangle + \|\downarrow_i\uparrow_j\uparrow_k\rangle)$
$\|\frac{3}{2},-\frac{1}{2}\,{}^e_{ijk}\rangle$	$\frac{1}{\sqrt{3}}(\|\downarrow_i\downarrow_j\uparrow_k\rangle + \|\downarrow_i\uparrow_j\downarrow_k\rangle + \|\uparrow_i\downarrow_j\downarrow_k\rangle)$
$\|\frac{3}{2},\frac{3}{2}\,{}^e_{ijk}\rangle$	$\|\uparrow_i\uparrow_j\uparrow_k\rangle$
$\|\frac{3}{2},-\frac{3}{2}\,{}^e_{ijk}\rangle$	$\|\downarrow_i\downarrow_j\downarrow_k\rangle$
$\|\frac{1}{2}t,\frac{1}{2}\,{}^e_{ijk}\rangle$	$\sqrt{\frac{2}{3}}\|\uparrow_i\uparrow_j\downarrow_k\rangle - \frac{1}{\sqrt{6}}\|\uparrow_i\downarrow_j\uparrow_k\rangle + \frac{1}{\sqrt{6}}\|\downarrow_i\uparrow_j\uparrow_k\rangle$
$\|\frac{1}{2}t,-\frac{1}{2}\,{}^e_{ijk}\rangle$	$\sqrt{\frac{2}{3}}\|\uparrow_i\uparrow_j\downarrow_k\rangle + \frac{1}{\sqrt{6}}\|\downarrow_i\uparrow_j\downarrow_k\rangle - \frac{1}{\sqrt{6}}\|\uparrow_i\downarrow_j\downarrow_k\rangle$
$\|\frac{1}{2}s,\frac{1}{2}\,{}^e_{ijk}\rangle$	$\frac{1}{\sqrt{2}}(\|\uparrow_i\uparrow_j\downarrow_k\rangle - \|\uparrow_i\downarrow_j\uparrow_k\rangle)$
$\|\frac{1}{2}s,-\frac{1}{2}\,{}^e_{ijk}\rangle$	$\frac{1}{\sqrt{2}}(\|\downarrow_i\downarrow_j\uparrow_k\rangle - \|\downarrow_i\uparrow_j\downarrow_k\rangle)$

APPENDIX B: NOTATION USED FOR THE STATE VECTORS

In Table III, we list the symbols and abbreviations used in writing the spin state vectors.

*poem@tx.technion.ac.il

[1] A. Hartmann, Y. Ducommun, E. Kapon, U. Hohenester, and E. Molinari, Phys. Rev. Lett. **84**, 5648 (2000).
[2] E. Dekel, D. Gershoni, E. Ehrenfreund, J. M. Garcia, and P. M. Petroff, Phys. Rev. B **61**, 11009 (2000).
[3] J. J. Finley, A. D. Ashmore, A. Lemaître, D. J. Mowbray, M. S. Skolnick, I. E. Itskevich, P. A. Maksym, M. Hopkinson, and T. F. Krauss, Phys. Rev. B **63**, 073307 (2001).
[4] B. Urbaszek, R. J. Warburton, K. Karrai, B. D. Gerardot, P. M. Petroff, and J. M. Garcia, Phys. Rev. Lett. **90**, 247403 (2003).
[5] R. Seguin, A. Schliwa, S. Rodt, K. Pötschke, U. W. Pohl, and D. Bimberg, Phys. Rev. Lett. **95**, 257402 (2005).
[6] D. V. Regelman, U. Mizrahi, D. Gershoni, E. Ehrenfreund, W. V. Schoenfeld, and P. M. Petroff, Phys. Rev. Lett. **87**, 257401 (2001).
[7] N. Akopian, N. H. Lindner, E. Poem, Y. Berlatzky, J. Avron, D. Gershoni, B. D. Gerardot, and P. M. Petroff, Phys. Rev. Lett. **96**, 130501 (2006).
[8] B. B. Blinov, D. L. Moehring, L. M. Duan, and C. Monroe, Nature (London) **428**, 153 (2004).
[9] M. E. Ware, E. A. Stinaff, D. Gammon, M. F. Doty, A. S. Bracker, D. Gershoni, V. L. Korenev, Ş. C. Bădescu, Y. Lyanda-

Geller, and T. L. Reinecke, Phys. Rev. Lett. **95**, 177403 (2005).
[10] R. J. Warburton, C. Schäflein, D. Haft, F. Bickel, A. Lorke, K. Karrai, J. M. Garcia, W. Schoenfeld, and P. M. Petroff, Nature (London) **405**, 926 (2000).
[11] M. Bayer, G. Ortner, O. Stern, A. Kuther, A. A. Gorbunov, A. Forchel, P. Hawrylak, S. Fafard, K. Hinzer, T. L. Reinecke, S. N. Walck, J. P. Reithmaier, F. Klopf, and F. Schafer, Phys. Rev. B **65**, 195315 (2002).
[12] S. Alon-Braitbart, E. Poem, L. Fradkin, N. Akopian, S. Vilan, E. Lifshitz, E. Ehrenfreund, D. Gershoni, B. D. Gerardot, A. Badolato, and P. M. Petroff, Physica E (Amsterdam) **32**, 127 (2006).
[13] L. Besombes, J. J. Baumberg, and J. Motohisa, Phys. Rev. Lett. **90**, 257402 (2003).
[14] D. Gammon, E. S. Snow, B. V. Shanabrook, D. S. Katzer, and D. Park, Phys. Rev. Lett. **76**, 3005 (1996).
[15] V. D. Kulakovskii, G. Bacher, R. Weigand, T. Kümmell, A. Forchel, E. Borovitskaya, K. Leonardi, and D. Hommel, Phys. Rev. Lett. **82**, 1780 (1999).
[16] N. Le Thomas, E. Herz, O. Schöps, and U. Woggon, Phys. Rev. Lett. **94**, 016803 (2005).
[17] A. Högele, M. Kroner, S. Seidl, K. Karrai, M. Atatüre, J. Dreiser, A. Imamoglu, R. J. Warburton, A. Badolato, B. D. Gerardot, and P. M. Petroff, Appl. Phys. Lett. **86**, 221905 (2005).
[18] S. Cortez, O. Krebs, S. Laurent, M. Senes, X. Marie, P. Voisin, R. Ferreira, G. Bastard, J.-M. Gérard, and T. Amand, Phys. Rev. Lett. **89**, 207401 (2002).
[19] A. Barenco and M. A. Dupertuis, Phys. Rev. B **52**, 2766 (1995).
[20] E. L. Ivchenko and G. E. Pikus, *Superlattices and Other Heterostructures*, Springer Series in Solid State Sciences Vol. 110 (Springer Verlag, Berlin, 1997).
[21] I. A. Akimov, K. V. Kavokin, A. Hundt, and F. Henneberger, Phys. Rev. B **71**, 075326 (2005).
[22] J. M. Garcia, T. Mankad, P. O. Holtz, P. J. Wellman, and P. M. Petroff, Appl. Phys. Lett. **72**, 3172 (1998).
[23] G. Ramon, U. Mizrahi, N. Akopian, S. Braitbart, D. Gershoni, T. L. Reinecke, B. D. Gerardot, and P. M. Petroff, Phys. Rev. B **73**, 205330 (2006).
[24] E. Dekel, D. Gershoni, E. Ehrenfreund, D. Spektor, J. M. Garcia, and P. M. Petroff, Phys. Rev. Lett. **80**, 4991 (1998).
[25] J. D. Jackson, *Classical Electrodynamics*, 3rd ed. (Wiley, New York, 1999).
[26] M. E. Ware, A. S. Bracker, E. Stinaff, D. Gammon, D. Gershoni, and V. L. Korenev, Physica E (Amsterdam) **26**, 55 (2005).
[27] M. Ediger, G. Bester, B. D. Gerardot, A. Badolato, P. M. Petroff, K. Karrai, A. Zunger, and R. J. Warburton, Phys. Rev. Lett. **98**, 036808 (2007).
[28] E. L. Ivchenko, *Optical Spectroscopy of Semioconductor Nanostructures* (Alpha Science, Oxford, 2005).
[29] T. Takagahara, Phys. Rev. B **62**, 16840 (2000).
[30] P. Y. Yu and M. Cardona, *Fundamentals of Semiconductors: Physics and Material Properties*, 3rd ed. (Springer, Berlin, 2001).
[31] D. Gershoni, C. H. Henry, and G. A. Baraff, IEEE J. Quantum Electron. **29**, 2433 (1993).
[32] *Physics of Group IV Elements and III-V Compounds*, edited by O. Madelung, M. Schulz, and H. Weiss, Landolt-Börnstein, New Series, Vol. 17, Pt. A (Springer, Berlin, 1982).
[33] S. V. Gupalov, E. L. Ivchenko, and A. V. Kavokin, J. Exp. Theor. Phys. **86**, 388 (1998).
[34] C. Cohen-Tannoudji, B. Diu, and F. Laloe, *Quantum Mechanics* (Wiley-Interscience, New York, 1977).
[35] C. Pryor, Phys. Rev. B **57**, 7190 (1998).
[36] M. M. Glazov, E. L. Ivchenko, L. Besombes, Y. Leger, L. Maingault, and H. Mariette, Phys. Rev. B **75**, 205313 (2007).
[37] E. Poem (unpublished).
[38] C. H. Henry and K. Nassau, Phys. Rev. B **1**, 1628 (1970).
[39] V. K. Kalevich, I. A. Merkulov, A. Y. Shiryaev, K. V. Kavokin, M. Ikezawa, T. Okuno, P. N. Brunkov, A. E. Zhukov, V. M. Ustinov, and Y. Masumoto, Phys. Rev. B **72**, 045325 (2005).
[40] E. Dekel, D. V. Regelman, D. Gershoni, E. Ehrenfreund, W. V. Schoenfeld, and P. M. Petroff, Solid State Commun. **117**, 395 (2001).
[41] D. V. Regelman, E. Dekel, D. Gershoni, E. Ehrenfreund, A. J. Williamson, J. Shumway, A. Zunger, W. V. Schoenfeld, and P. M. Petroff, Phys. Rev. B **64**, 165301 (2001).
[42] M. M. Glazov, E. L. Ivchenko, R. V. Baltz, and E. G. Tsitsishvili, arXiv:cond-mat/0501635 (unpublished).
[43] W. Sheng, S.-J. Cheng, and P. Hawrylak, Phys. Rev. B **71**, 035316 (2005).